



**HAL**  
open science

## Ultrasonic-assisted oxidation of Cellulose to Oxalic acid over gold nanoparticles supported on iron-oxide

Prince Nana Amaniampong, Thang Trinh, Teseer Bahry, Jia Zhang, François  
Jerome

► **To cite this version:**

Prince Nana Amaniampong, Thang Trinh, Teseer Bahry, Jia Zhang, François Jerome. Ultrasonic-assisted oxidation of Cellulose to Oxalic acid over gold nanoparticles supported on iron-oxide. *Green Chemistry*, 2022, 24 (12), pp.4800-4811. 10.1039/D2GC00433J . hal-03845508

**HAL Id: hal-03845508**

**<https://hal.science/hal-03845508v1>**

Submitted on 21 Nov 2023

**HAL** is a multi-disciplinary open access archive for the deposit and dissemination of scientific research documents, whether they are published or not. The documents may come from teaching and research institutions in France or abroad, or from public or private research centers.

L'archive ouverte pluridisciplinaire **HAL**, est destinée au dépôt et à la diffusion de documents scientifiques de niveau recherche, publiés ou non, émanant des établissements d'enseignement et de recherche français ou étrangers, des laboratoires publics ou privés.

# Ultrasonic-assisted oxidation of Cellulose to Oxalic acid over gold nanoparticles supported on iron-oxide

Received 00th January 20xx,  
Accepted 00th January 20xx

DOI: 10.1039/x0xx00000x

Prince Nana Amaniampong,<sup>\*[a]</sup> Quang Thang Trinh,<sup>\*[b]</sup> Teseer Bahry,<sup>[a]</sup> Jia Zhang,<sup>[b]</sup> François Jérôme<sup>[a]</sup>

The use of unconventional activation techniques, such as low frequency ultrasound (US), in combination with heterogeneous catalysts offers a powerful synergistic approach to transform renewable resources to value added chemicals. In this context, we report a catalytic base-free strategy for the selective oxidation of microcrystalline cellulose to oxalic acid (OA) by combining low frequency ultrasound and Au/Fe<sub>2</sub>O<sub>3</sub> as a catalyst. We demonstrate that low frequency ultrasound induces the fragmentation of cellulose particles, making it more prone to catalytic oxidation in the presence of Au/Fe<sub>2</sub>O<sub>3</sub>. Under optimized conditions, OA was obtained with 45% yield in the presence of molecular oxygen, corresponding to an overall yield of 53% into carboxylic acids (gluconic, formic, 2-keto-gluconic acid, etc). Furthermore, by means of Density Functional Theory, it was demonstrated that a charge transfer occurred from Au nanoparticles to Fe<sub>2</sub>O<sub>3</sub>, resulting in the formation of active catalytic species capable of decomposing H<sub>2</sub>O<sub>2</sub>, formed by sonolysis of water, to reactive O\* species that were involved in the oxidation of cellulose. This charge transfer was also highlighted by X-ray photoelectron spectroscopy which revealed a partial oxidation of Au<sup>0</sup> to Au<sup>3+</sup>.

## Introduction

Oxalic acid (OA), a soluble dicarboxylic acid, is an industrially relevant platform chemical with applications in the synthesis of renewable polymers,<sup>1, 2</sup> extraction of rare earths from manozite, leather manufacturing, celluloid production and in the synthesis of pharmaceutical intermediates.<sup>3</sup> From 2001, the world market for OA saw a steady increase at an annual rate of 3.15 %, mainly boosted by the worldwide growing demand of our society for polymers. As a result, the consumption of OA has reached 278 thousand tons in 2010, as was reported by Global Industry Analysts, Inc.<sup>4</sup> From 2012 to 2016, the annual growth rate of OA has even

reached ~10 %, with the Asia region being the world's largest market. Conventionally, most of oxalic acid is synthesized through chemical processes which includes oxidation of olefins and glycols, oxidation of carbohydrates with trioxonitrate (v) acid, decomposition of formates followed by tetraoxosulphate (vi) acid treatment,<sup>5</sup> among the most well-known routes. Unfortunately, these chemical processes have been reported to be eco-harmful because of a complicated downstream processing. Hence, the search of alternative and more efficient routes, in terms of atom economy and waste prevention, is of high industrial interest. In this context, the specific development of heterogeneous catalysts for the synthesis of OA from biomass has garnered much attention. However, these heterogeneously-catalyzed pathways to OA are still facing important scientific hurdles such as poor product selectivity/yield and, in many cases, a poor stability and activity of heterogeneous catalysts under the working conditions. For instance, using a cobalt-based catalyst, in the presence of molecular oxygen, Jin *et al.*<sup>6</sup> reported an OA yield of 24 % from glycerol. Though it was encouraging, their cobalt-based catalyst

<sup>a</sup> Institut de Chimie des Milieux et Matériaux de Poitiers, University of Poitiers, CNRS 1 rue Marcel Doré, 86073 Poitiers, France. E-mail : prince.nana.amaniampong@univ-poitiers.fr

<sup>b</sup> Institute of High Performance Computing, A\*STAR (Agency for Science, Technology and Research), 1 Fusionopolis Way #16-16 Connexis, 138632 Singapore. E-mail : trinqt@ihpc.a-star.edu.sg

† Footnotes relating to the title and/or authors should appear here.

Electronic Supplementary Information (ESI) available: [details of any supplementary information available should be included here]. See DOI: 10.1039/x0xx00000x

demonstrated a preferential product yield towards tartronic acid (64 %).<sup>6</sup> Reactions that utilized bimetallic<sup>6-9</sup> and trimetallic<sup>10, 11</sup> systems of noble metal catalysts, with the purpose of enhancing the activity and stability of the catalyst, also suffer from a lack of selectivity, with OA being formed with only 20% yields at 80% conversion of glycerol. A similar result was reported using a layered double hydroxide (LDH) hosted transition metal complexes (LDH-[MnSO<sub>3</sub>-salphen]) as catalyst.<sup>9</sup> Although much efforts have been paid to the synthesis of OA from biobased glycerol, the low selectivity towards OA and the public perception on food *versus* energy/chemicals makes however the use of glycerol (a main co-product of the vegetable oil and biodiesel industry) for the fabrication of chemicals a critical point, despite the expected tonnages are rather low. In this context, the synthesis of OA has been also explored from cellulosic biomass waste, in particular by alkali fusion or nitric acid oxidation processes. However, the nitric acid oxidation process often requires high nitric acid concentrations (*ca.* 40 wt%), which unfortunately hampers the implementation of this process on a large scale, mainly due to corrosive issues and important investment costs associated to the need of special reaction apparatus.<sup>12</sup> Similarly, alkali process, *i.e.* immersion of cellulosic biomass waste in alkaline solutions at high temperatures (> 200 °C), also required a high concentration of NaOH (> 16 N NaOH) to get ~66 % yield of OA within 12 h of reaction time, again making it difficult the industrial deployment of this route.<sup>13, 14</sup> These harsh conditions are required to overcome the recalcitrance of cellulose to chemical processing, due to its complex inter- and intramolecular hydrogen bond network, which renders its depolymerization and conversion to OA a very difficult task. To activate cellulose, the development of alternative technologies that can potentially dislodge the recalcitrant crystalline structure of cellulose and render it more reactive for chemical processing is in vogue. For instance, the use of non-thermal atmospheric plasma,<sup>15</sup> ball-milling,<sup>16</sup> microwave,<sup>17</sup> etc., has been demonstrated to be emerging technologies for promoting the depolymerization of cellulose, either with or without a catalyst.

Ultrasound has also been investigated for the depolymerization of cellulose and the pre-treatment of lignocellulosic biomass. The chemical and physical advantages of ultrasound irradiation rely on cavitation phenomena, *i.e.* the formation, growth and implosion of cavitation bubbles which induce either physical or chemical effects,

depending on the applied ultrasonic frequency. Low frequency ultrasounds (<80 kHz) mainly induce physical effects (shock waves, micro-jets, turbulences, etc). The shockwaves and high-speed microjets impacts, that accompanies the production of radicals during ultrasonic cavitation implosion, can destroy or loosen the chemical linkages in the lignocellulosic structures, resulting in the release of short fragments that can be further processed into valuable chemicals.<sup>18</sup> For instance, a report from Sun *et al.*<sup>19</sup> revealed that 77% of lignin and 41% of hemicellulose were extracted from wheat straw after 20 min of ultrasonic-assisted extraction at 60°C in an aqueous and basic (NaOH, 0.5 M) solution of methanol (60 wt%). A similar result was reported by Velmurugan and Muthukumar,<sup>20</sup> and Garcia *et al.*,<sup>21</sup> using sugarcane bagasse and olive tree biomass as substrates, where the application of a sono-assisted alkaline pre-treatment led to the liberation and depolymerisation of hemicellulose and lignin.<sup>21</sup> Using a microcrystalline cellulose, Zhiwei *et al.* reported an oxalic acid yield of 41.5 % over a CuO catalyst in an alkaline environment at an oxygen pressure of 0.3 MPa and reaction temperature of 200 °C.<sup>22</sup> The group also investigated the catalytic activity of Co<sub>2</sub>O<sub>3</sub>, Fe<sub>2</sub>O<sub>3</sub>, CeO<sub>2</sub> and MnO<sub>2</sub> metal oxide catalysts, and report oxalic acid yields of 17 %, 15 %, 17 % and 10 %, respectively under the same reaction conditions described for the reaction performed over CuO catalyst. In combination with a catalyst, the selectivity of involved sonochemical reactions can be more easily controlled, potentially leading to the formation of biobased and valuable products that are hitherto difficult to obtain by conventional catalytic reactions.<sup>23, 24</sup> For example, while glucose is conventionally oxidized to gluconic acid, glucose can be selectively oxidized into glucuronic acid by coupling iron sulfate or CuO with low (100 kHz) and high frequency (550 kHz) ultrasound, respectively.<sup>25, 26</sup>

Here we investigate the coupling of low frequency ultrasound with catalysis (Au/ Fe<sub>2</sub>O<sub>3</sub>) in the selective oxidation of cellulose to OA. We show that the intense shock-waves and energy that are locally generated at the bubble collapse time led to a partial fragmentation of cellulose particles, making it more reactive with the Au/Fe<sub>2</sub>O<sub>3</sub> catalyst. Furthermore, through a combined experimental and theoretical investigations, we propose a plausible reaction mechanism where H<sub>2</sub>O<sub>2</sub>, formed *in situ* by sonolysis of water, is converted to reactive O\* species at the Au-Fe<sub>2</sub>O<sub>3</sub> interface, inducing the oxidation of cellulose to OA.



## Materials and Methods

**Materials.** Microcrystalline cellulose (Avicel PH200, FMC Biopolymer) was utilized as substrate. d-(+)-Glucose (>99.5 %), d-(+)-Fructose (>99.5 %), d-(+)-Cellobiose (>98%), Oxalic acid (98 %) were all purchased from Sigma–Aldrich.

**Catalyst.** 1.0 wt. % Au/Fe<sub>2</sub>O<sub>3</sub> catalyst was used as received from Sued-Chemie Catalysts Japan (World gold council, gold reference catalyst sample No: 34C).

**Catalyst Characterization.** X-ray spectroscopic (XPS) analysis was performed on a Thermo Escalab 250 spectrometer. The binding energy was calibrated using C 1s value of 284.6 eV as a reference.

**Ultrasound-assisted catalytic conversion of microcrystalline cellulose.** The sonochemical oxidative conversion of cellulose was performed in a 25 mL batch reactor (image of the sonochemical batch reactor is shown in Supporting information). Cellulose (typically 0.2 g) and catalyst (0.025g) were added to the reactor pre-charged with deionized H<sub>2</sub>O. Air was first purged from the reactor by pressurizing and de-pressurizing several times with pure O<sub>2</sub> before adjusting the O<sub>2</sub> pressure to the desired value. The suspension was then subjected to an ultrasonic irradiation at 20 kHz for 1-9 hours. After 9 h of reaction, the reactor was cooled down to room temperature and the products were analysed by HPLC.

**Analytical Methods.** The amounts of oxalic acid and other acid products were determined from the HPLC analysis by using a Shimadzu SPD-20A HPLC equipped with an ICE-COREGEL 107 H column 300 × 7.8 mm from Transgenomic, a UV/Vis detector (SPD-20A, 210 nm) and a refractive index detector (LC-20AD). A H<sub>2</sub>SO<sub>4</sub> aqueous solution (0.01 M) was used as the eluent at a flow rate of 0.8 mL.min<sup>-1</sup>. External calibration was performed using standards of oxalic acid, cellobiose, fructose, acetic acid, glucuronic acid gluconic acid and 2-keto-gluconic acid. Cellulose conversion was determined based on weight difference of cellulose before and after reaction.

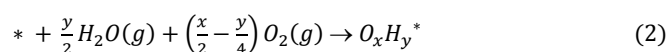
$$Conv (\%) = \frac{M_o - M_f}{M_o} \times 100 \%$$

where M<sub>o</sub> is the initial mass of cellulose and M<sub>f</sub> is the mass of cellulose after reaction. Yield of organic acids were determined by;

$$Yield (\%) = \frac{\text{moles of carbon in organic acid}}{\text{moles of carbon in feedstock}} \times 100 \%$$

**Computational details.** All the Density Functional Theory (DFT) calculations were performed using a plane-wave basis set with a cut-off kinetic energy of 450 eV and the projector-augmented wave (PAW) scheme implemented in the ab-initio total-energy and molecular-dynamics program VASP (Vienna ab-initio simulation program) developed at the Fakultät für Physik of the Universität Wien.<sup>27, 28</sup> To correct for the self-interaction error in strongly correlated systems such as Fe<sub>2</sub>O<sub>3</sub>,<sup>29</sup> we employed a Hubbard correction of U = 4.3 eV within the PBE+U exchange correlation functional, which described appropriately the band gap and bulk lattice parameters of Fe<sub>2</sub>O<sub>3</sub> as reported in earlier studies.<sup>30, 31</sup> All calculations involving Fe<sub>2</sub>O<sub>3</sub> structures were spin-polarized with the antiferromagnetic ordering, and the Grimme's D3 approach was included to correct the long-range dispersion interactions.<sup>32</sup> Fe<sub>2</sub>O<sub>3</sub> support was modelled using the oxygen-terminated (3×1) Fe<sub>2</sub>O<sub>3</sub>(0001) surface (including 6 layers of Fe atoms and 7 layers of O atoms), which was reported as the most stable exposed surface of Fe<sub>2</sub>O<sub>3</sub> under the similar reaction conditions applied in this study.<sup>33-35</sup> A k-point grid density of 4×2×1 was used to sample the Brillouin zone for all the calculations on Fe<sub>2</sub>O<sub>3</sub> systems. To evaluate the interaction between Au nanoparticle and the Fe<sub>2</sub>O<sub>3</sub> support and understand the formation of different active oxidize agents on the Au/Fe<sub>2</sub>O<sub>3</sub> catalyst, several models were studied: Au overlayer films on Fe<sub>2</sub>O<sub>3</sub> (0001) surface; Au nanorod on Fe<sub>2</sub>O<sub>3</sub> (0001) surface and pure Au (111) surface. More details of those model structures and computational procedures were presented in the Supporting Information.

To evaluate the affinity of different oxidize agents generated by the Au/Fe<sub>2</sub>O<sub>3</sub> catalyst (H\*, O\*, O<sub>2</sub>, OH\*, OOH\* and H<sub>2</sub>O<sub>2</sub>), we computed their binding energies as the formation energy of the reaction in equation (2):



wherein \*, H<sub>2</sub>O(g) and O<sub>2</sub>(g) are the clean surface; H<sub>2</sub>O and O<sub>2</sub> in gas phases, respectively. Furthermore, to understand the electronic properties of Au/Fe<sub>2</sub>O<sub>3</sub> interfacial site and the chemical perturbation of those interfacial Au site at different proximity from the substrate, we computed the adhesion energies (ΔE<sub>adh</sub>) and charge density difference (Δρ) for the Au(111) overlayer films on Fe<sub>2</sub>O<sub>3</sub> (denoted as Au<sub>n</sub>/Fe<sub>2</sub>O<sub>3</sub>) with different Au thicknesses (one, two and three overlayers) using the equations (3) and (4) below.

The Bader charges of all atoms in those structures were also computed using the approach by Henkelman et al.<sup>36, 37</sup>

$$\Delta E_{adh} = \frac{E_{Au_n/Fe_2O_3} - E_{Fe_2O_3} - nE_{Au(g)}}{n} \quad (3)$$

where  $E_{Au_n/Fe_2O_3}$ ,  $E_{Fe_2O_3}$  and  $E_{Au_{gas}}$  are the total energies of Au over-layers supported on  $Fe_2O_3$ ; total energy of clean  $Fe_2O_3$  and the total energy of one Au atom in gas phase, respectively.

$$\Delta\rho = \rho_{Au_n/Fe_2O_3} - \rho_{Fe_2O_3} - \rho_{Au_n} \quad (4)$$

where  $\rho_{Au_n/Fe_2O_3}$ ,  $\rho_{Fe_2O_3}$  and  $\rho_{Au_n}$  are the charge densities of the Au overlayers supported on  $Fe_2O_3$ , clean  $Fe_2O_3$  and  $Au_n$  cluster, respectively.

## RESULTS AND DISCUSSION

In a first set of experiments, we explored the catalyst-free sonochemical conversion of cellulose at 20 kHz in deionized water and under different gas atmospheres, at a pressure of 0.15 MPa. With our ultrasonic equipment, it was unfortunately not possible to monitor the temperature inside the reactor. However, using an infra-red temperature gun, the outside temperature of the reactor was measured at 80 °C during our experiments, suggesting that much higher temperatures were reached inside the ultrasonic reactor.

As shown in **Figure 1**, product analysis revealed only trace amount of oxalic acids (<8 % yield).  $O_2$  gas led to a slightly higher yield in OA (~8 %) as compared to the yields obtained under Ar (~5%), He (~2 %),  $H_2$  (~2%) and Ar/ $O_2$  mixture (~5%).

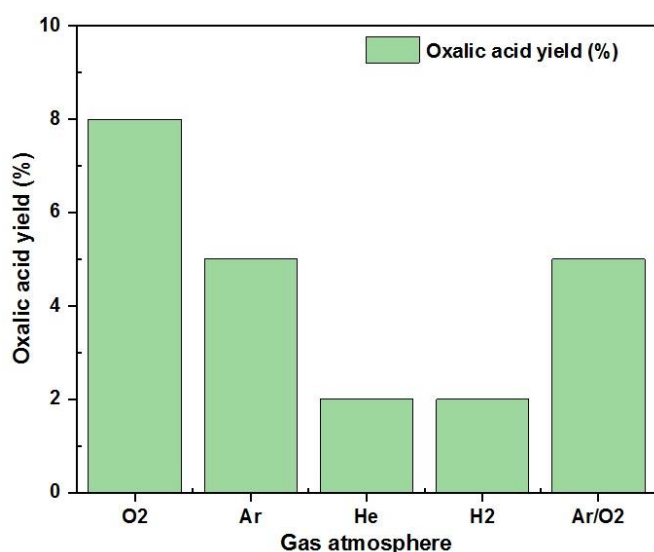


**Figure 1.** Effect of gas atmosphere on the catalyst-free conversion of cellulose to oxalic acid under ultrasonic irradiation. Reaction conditions: 0.2g Cellulose, 15 mL water, 0.15 MPa gas pressure, 9 h reaction time.

Next,  $Fe_2O_3$  was added into the ultrasonic reactor.  $Fe_2O_3$  has been selected owing to its abundant availability, cheap costs and known high activity in oxidation of biomass.<sup>26, 38, 39</sup> Addition of  $Fe_2O_3$  in the ultrasonic reactor, while keeping constant all other parameters (0.2g Cellulose, 15 mL water, 0.15 MPa gas pressure), led to OA in 10% yield, after 9 h of ultrasonic irradiation. This result was not very different from those obtained under catalyst-free conditions, suggesting the inability of  $Fe_2O_3$  to oxidize cellulose under our working conditions (**Figure 1**). Owing to their proven excellent oxidation abilities at the nanoscale, gold nanoparticles were next deposited on the  $Fe_2O_3$  catalyst support and its catalytic activity on the conversion of cellulose under ultrasonic irradiation was then investigated. Products selectivity and yields were determined at a reaction time span of 1-9 h, using the Au/ $Fe_2O_3$  catalyst (**Figure 2**), and at a fixed  $O_2$  pressure of 0.15 MPa. Full characterization of the Au/ $Fe_2O_3$  catalyst is provided in the SI. In the presence of the Au/ $Fe_2O_3$  catalyst, a steady increase in cellulose conversion was observed from ~10 % to ~ 55%, after 1 and 9 h of ultrasonic irradiation time, respectively, with a corresponding OA yields of 2 % and 45 %, respectively. Gluconic acid (~2 %) and 2-*keto*-Gluconic acid (~6 %) were observed as main co-products. Again, in the presence of the Au/ $Fe_2O_3$  catalyst, we investigated the effect of the gas atmosphere on the OA yield. To this end,  $O_2$  was replaced by Ar (kinetic investigations are presented in the SI). Interestingly, the OA yield was decreased from 45% under  $O_2$  to only ~18 % (after 10 h) yield under Ar. These results emphasize the importance of oxygen atmosphere in enhancing the yield of OA, during the irradiation of cellulose. The carbon balance was analysed alongside the formation of organic acids. After 4 h of reaction time, there was an observed drop of carbon balance from 100 to 95 %, which further dropped to 85 % after 9 h of reaction. At this point, we passed the depressurised gas at the headspace of the reactor after reaction through a solution of calcium hydroxide. The solution turned milky, suggesting the presence of  $CO_2$  which was formed as a results of C-C of organic acid products. Noteworthy, we did not quantify the concentration of  $CO_2$  as it was beyond the scope of this current study.

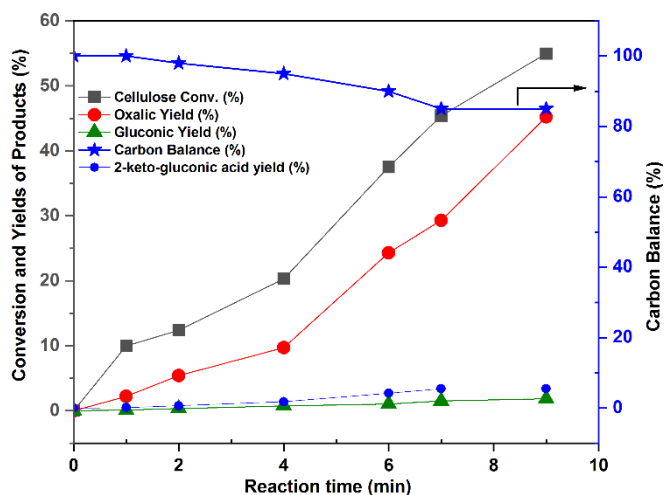


**Figure 2.** Ultrasonic irradiation time course and carbon balance for cellulose conversion over Au/Fe<sub>2</sub>O<sub>3</sub> catalyst. Reaction conditions: 0.2g Cellulose, 15 mL water, 0.025 g Au/Fe<sub>2</sub>O<sub>3</sub>.

The effect of the O<sub>2</sub> pressure on the yields of organic acids, including OA, was studied by varying the pressure of O<sub>2</sub> from 0.05 to 0.25 MPa (Figure 3). Reactions were conducted under ultrasonic irradiation for 9 h. At an oxygen pressure of 0.05 MPa, a cellulose conversion of 45 % and an OA yield of 29 %, together with the formation of gluconic acid (10 % yield) and 2-keto-gluconic acid (15 % yield), were observed. Upon increasing the pressure of oxygen to 0.1 MPa, a slight increase in the conversion of cellulose (48 %) was noticed, along with an increase in the yield of OA (~35 %) and a concomitant decrease in the yields of gluconic (8 %) and 2-keto-gluconic acid (10 %), respectively. A similar trend was observed when the pressure was further increased to 0.15 MPa. In this case, a cellulose conversion of 55 %, along with the formation of OA with a yield of 45 %, were obtained. In this latter case, the yields of gluconic acid and 2-keto-gluconic further decreased to 2 % and 6 % yields, respectively, suggesting that these chemicals are intermediate species. Interestingly, the pressure of O<sub>2</sub> did not impact significantly the conversion of cellulose observed after 9 h of reaction (from 45% at 0.05 MPa to 55% at 0.15 MPa), indicating that the O<sub>2</sub> pressure exerted a minor effect on the reaction rate. On the contrary, the selectivity to OA was significantly impacted by the pressure of O<sub>2</sub>. Indeed, going from 0.05 to 0.15 MPa of O<sub>2</sub>, the selectivity to OA gradually increased from 64% to 82%. Considering that the conversion of cellulose is quite close at these three O<sub>2</sub> pressures (45-55%), it indicates that O<sub>2</sub> impacted to some extent the reaction mechanism.

In line with our observations, a further increase of the O<sub>2</sub> pressure from 0.15 to 0.25 MPa did not significantly impacted the conversion of cellulose (55 to 58%). However, at 0.25 MPa, the selectivity to OA dropped to 60% (vs 82% at 0.15 MPa) and formic acid was identified as a secondary product (10% yield), presumably due to over-oxidation reactions. Therefore, it suggests that the selectivity to OA is a compromise between the O<sub>2</sub> pressure and the reaction time.

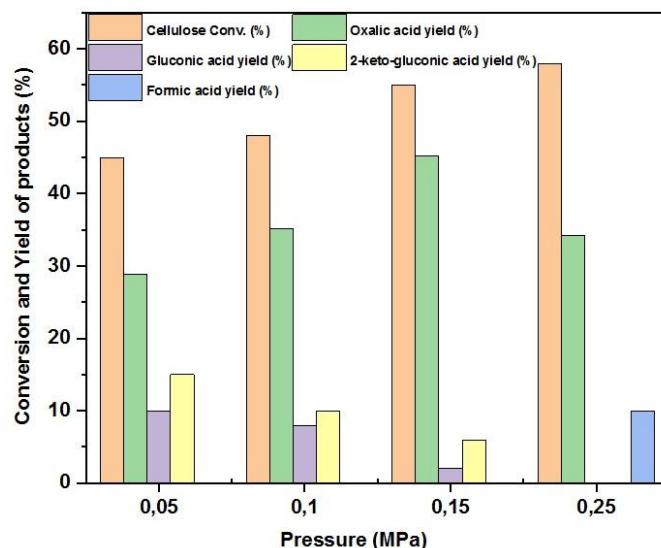


**Figure 3.** O<sub>2</sub> pressure effect on the conversion of cellulose to oxalic acid under ultrasonic irradiation. Reaction conditions: 0.2 g Cellulose, 15 mL water, 0.025 g Au/Fe<sub>2</sub>O<sub>3</sub>, 9 h reaction time.

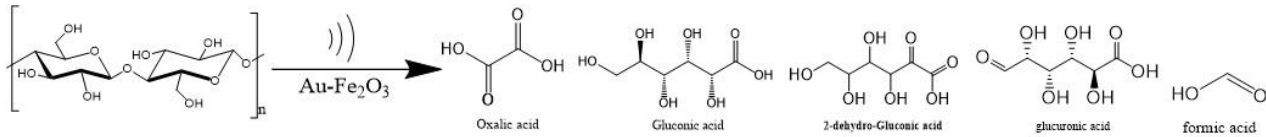
#### Scope of the reaction and first mechanism insights

In order to get first insights on the reaction mechanism, other carbohydrates were tested. First, glucose was tested as a substrate (Table 1, entry 1 and 2). In this case, gluconic acid was observed as the major product (~ 41% yield) after 2 h of ultrasonic irradiation, together with the formation of small amounts of glucuronic acid (~ 7% yield), 2-keto-gluconic acid (9 % yield), oxalic acid (~ 3% yield) and trace amounts of formic acid (< 1% yield). When the ultrasonic time was extended from 2 to 4 h, gluconic and 2-keto-gluconic acid yields (Table 1, entry 2) were reduced, which was accompanied by a concomitant increase of the OA yield to 32 %. These results confirmed that gluconic and 2-keto-gluconic acids are intermediates species in the formation of OA. To further confirm this, gluconic acid was used as a reaction substrate in the oxidation reaction (Table 1, entry 3-5). OA was formed with ~37 % yield after 2 h of irradiation time (*i.e.* 60 % conversion of gluconic acid) together with the formation of 21 % of 2-keto-gluconic acid and trace amount of formic acid (~ 2%). Upon extension of the irradiation time from 2 to

4 h and then 6 h, the OA yield gradually increased from 37% to ~54% and 59%, respectively. Concomitantly, the yield of 2-keto-gluconic acid decreased from 21% to only 4% (4 h) and then even 0% at 6 h, while the yield in formic acid increased from 2% to 17% (4 h) and then 26% (6h). These results confirm that (i) gluconic acid is an intermediate species in the formation of OA and (ii) that extended ultrasonic irradiation time led to an over-oxidation of OA to formic acid. It is noteworthy that a similar result was obtained from fructose, indicating that possible isomerization of glucose to fructose might not be an issue in this process (ESI). Then, we

focused our attention on cellobiose, a dimeric model compound for cellulose (Table 1, entry 6). The formation of OA from cellobiose proceeded also very well, indicating that the  $\beta$ -1,4 glycosidic bond was rapidly cleaved under ultrasonic irradiation. Indeed, under pressure of  $O_2$  (0.15 MPa), (Table 1, entry 6) OA was formed with ~82% yield after 6 h of irradiation, with an almost complete conversion of cellobiose (98%). As above observed with cellulose, lower yields of OA were however observed when the gas atmosphere was changed to Ar, highlighting again the important role of  $O_2$  on the reaction mechanism (ESI).

**Table 1** Product yields for the Au/Fe<sub>2</sub>O<sub>3</sub> catalyzed sonochemical oxidation of model substrates.



Substrate	Gas atmosphere	Reaction time (h)	Conversion (%)	Oxalic acid	Gluconic acid	2-keto-gluconic acid	Glucuronic acid	Formic acid	Acetic acid
Glucose	Oxygen	2	58	3.3	40.9	9.0	6.9	0.8	0
		4	64	31.7	6.2	1.8	12.8	22.2	0
Gluconic acid		2	60	36.7	-	21.4	0	1.6	0
		4	78	53.8	-	4.3	0	16.9	0
		6	86	59.4	-	0	0	25.6	0
Cellobiose		6	98	82.4	4.0	9.9	-	0	0
Cellulose <sup>a</sup>	6	20	2	12.9	0	0	0	0	
Cellulose <sup>b</sup>	6	30	9.4	5.5	0	0	0	3	
Glucose <sup>c</sup>	-	6	75	1.6	49.7	12.4	0	0	3.4
Cellobiose <sup>a</sup>	Oxygen	4	60	15	20	0.9	-	2	0

<sup>a</sup>Reactions condition: 0.200g of cellulose, 15 mL H<sub>2</sub>O, 1.0 MPa of O<sub>2</sub>, 6 h, 150 °C, 0.025g of Au/Fe<sub>2</sub>O<sub>3</sub>, reactions were performed in a high-pressure auto-clave reactor.

<sup>b</sup>Reaction conditions: 0.200g of recovered cellulose after ultrasound irradiation, 15 mL H<sub>2</sub>O, 1.0 MPa of O<sub>2</sub>, 6 h, 150 °C, 0.025g of Au/Fe<sub>2</sub>O<sub>3</sub>, reactions were performed in a high-pressure auto-clave reactor.

<sup>c</sup>Reaction conditions: 0.200g of glucose, 15 mL H<sub>2</sub>O, 1.0 equiv. H<sub>2</sub>O<sub>2</sub>, 6 h, 90 °C, 0.025g of Au/Fe<sub>2</sub>O<sub>3</sub>

<sup>a</sup>Reaction condition: 0.200 g of cellobiose, 15 mL H<sub>2</sub>O, 0.15 MPa of gas, No catalyst

In an attempt to get more information on the role of ultrasound, the oxidative depolymerisation of cellulose was conducted under silent conditions in an autoclave pressurized at 0.15 MPa of O<sub>2</sub>, and in the presence of the Au/Fe<sub>2</sub>O<sub>3</sub> catalyst. The temperature of the autoclave was set at 150°C. Under these conditions, no product was detected. However, when the pressure of O<sub>2</sub> was increased to 1

MPa, gluconic acid was formed with ~13% yield (Table 1, entry 7), with the formation of OA in trace amount (2% yield). These results indicate that, under silent conditions, the catalytic oxidative depolymerisation of cellulose to OA requires harsh conditions, which are probably locally obtained by the application of ultrasound at 20 kHz. In another experiment, cellulose was first pre-treated



under ultrasound (Reaction conditions: 0.2g Cellulose, 15 mL water, 0.15 MPa O<sub>2</sub> gas pressure) and then the recovered cellulose after ultrasonic irradiation was subjected to “classical” oxidation reaction in a high-pressure auto-clave reactor (Reaction conditions 15 mL H<sub>2</sub>O, 1.0 MPa of O<sub>2</sub>, 6 h, 150 °C, 0.025g of Au/Fe<sub>2</sub>O<sub>3</sub>). At these conditions, an OA yield of 9% was observed together with the formation of gluconic acid (~6 %) and acetic acid 3 % (Table 1, entry 8). Comparing these results to those obtained in Table 1, entry 7, it could be reasonably suggested that ultrasonic irradiation alters the recalcitrant structure of cellulose. In order to evaluate the effect of ultrasound in promoting the cleavage of the glycosidic bonds, a blank reaction (absence of catalyst) was performed where cellobiose was selected as the reaction substrate (reaction conditions: 0.200g of cellobiose, 15 mL H<sub>2</sub>O, 0.15 MPa of O<sub>2</sub>). Analysis by HPLC revealed an oxalic acid and gluconic acid yields of 15 % and 20 %, respectively, at a cellobiose conversion of 60 %, together with trace amounts of formic acid and 2-keto-gluconic acid (2 % and ~ 1% yields, respectively, after 4 h of reaction irradiation time).

To assess the effect of cavitation events on the cellulose conversion, the unreacted cellulose was recovered and analysed.<sup>40-</sup>

<sup>42</sup> XRD patterns of ultrasonically treated cellulose under oxygen or air (0.15 MPa) were strikingly similar to that of the XRD patterns of the starting cellulose (Figure 4). Indeed, according to the conventional peak intensity method, the calculated crystallinity index ( $I_{CR}$ ) values were  $75.5 \pm 0.2$  %,  $78.8 \pm 0.4$  % and  $71.8 \pm 0.1$  % for the starting cellulose and ultrasonically treated cellulose under O<sub>2</sub> or air, respectively indicating that the crystallinity of cellulose was not altered by ultrasound, a result in line with previous reports.<sup>43, 44</sup>

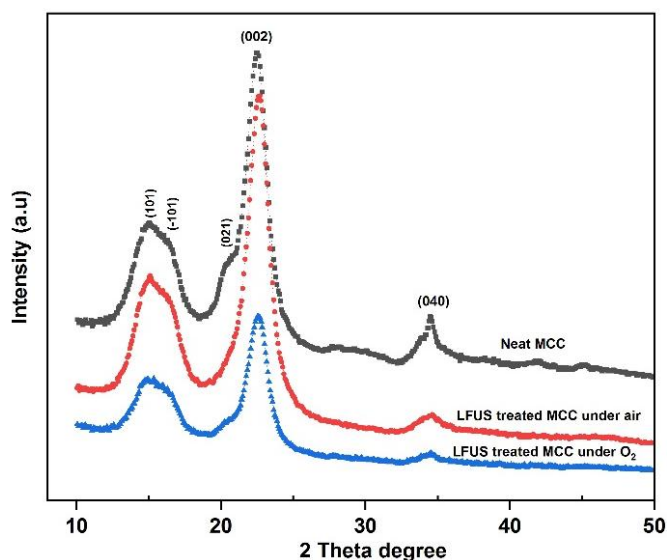


**Figure 4.** XRD patterns of cellulose before and after ultrasound treatment (0.2g cellulose, 15 mL water, 0.15 MPa O<sub>2</sub> pressure, 9 h reaction time).

Next, cellulose was subjected to ultrasonic irradiation (Reaction conditions: 0.2g Cellulose, 15 mL water, 0.15 MPa O<sub>2</sub> gas pressure, 9h reaction time) without any catalyst and the recovered cellulose was dried and analysed by scanning electron microscopic analysis (SEM) to assess the impact of ultrasound on the cellulose particles. SEM images of the starting and ultrasonically treated cellulose are shown in **Figures 5a and 5b**.

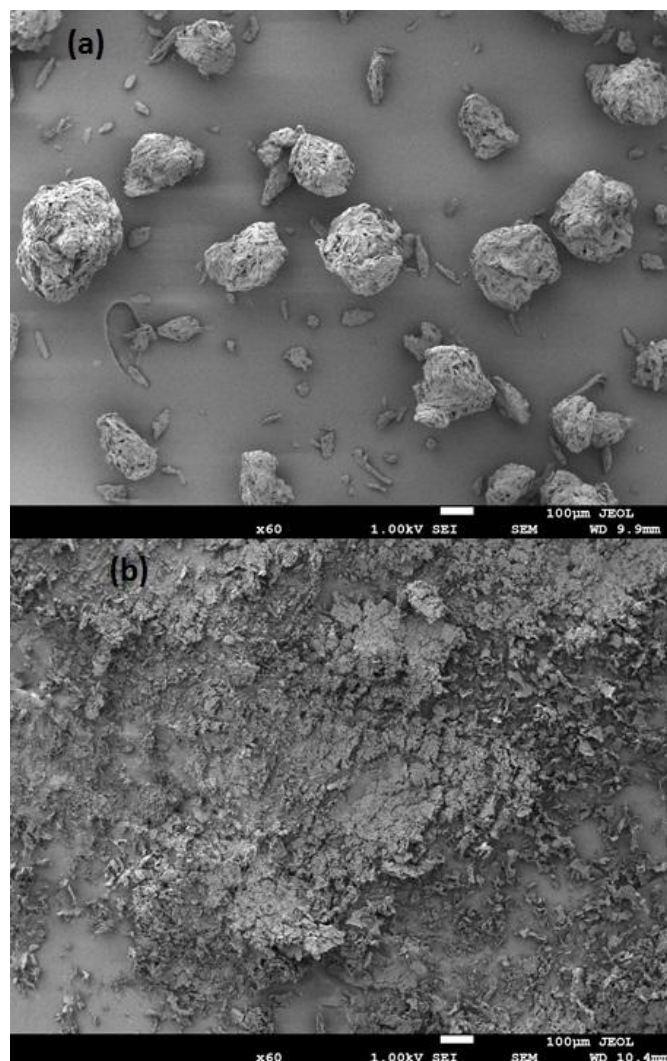


**Figure 5.** SEM images obtained for (a) neat cellulose (b) unreacted cellulose remaining after ultrasonic irradiation (Reaction conditions: 0.2g Cellulose, 15 mL water, 0.15 MPa gas pressure, 9 h reaction time).

The SEM images of the starting cellulose showed the agglomeration of lamellar-shaped structures into a ball-like cellulosic particles. In contrast, after ultrasonic irradiation, these ball-like structures were disorganized and reduced to much smaller particle sizes, presumably caused by the release of intense shock waves on the cellulosic particle surfaces at the bubble collapse time. It is noteworthy that without catalyst, this disaggregation of the cellulose particles induced by ultrasound under pressure of  $O_2$  was also accompanied by a release of short cellulosic fragments (degree of polymerization 1-13) in the aqueous phase (Figure S6, S1). Although their amount remains quite low (< 10% based on the conversion of cellulose), it provides additional evidence that, under pressure of  $O_2$ , ultrasound not only led to a fragmentation of cellulosic particles but also initiated first cleavages of the  $\beta$ -1,4

glycosidic bonds. From these results, we hypothesized that the reduction in cellulosic particle size and the partial cleavage of the  $\beta$ -1,4 glycosidic bonds greatly contribute to facilitate the reactivity of cellulose with the  $Au/Fe_2O_3$  catalyst.

It is known that during the ultrasonic irradiation of water, vapors of water trapped in the cavitation bubbles can be pyrolyzed to yield  $\bullet OH$  and  $\bullet H$  radicals. These radical species could also participate in the reaction mechanism. Indeed,  $\bullet OH$  and  $\bullet H$  radicals can recombine to form  $H_2O_2$  and  $H_2$ . Under  $O_2$  atmosphere, additional amount of  $H_2O_2$  can be formed due to the scavenging of radical  $\bullet H$  by  $O_2$  (formation of  $HO_2\bullet$  and then  $H_2O_2$ ).<sup>45</sup> As a result, we determined the amount of  $H_2O_2$  formed during ultrasound irradiation. To this end, pure water was sonicated at a controlled temperature of 80 °C and the formation of  $H_2O_2$  was monitored using a standardized spectro-photochemical method described in the ESI (Figure 6). After 30 min of irradiation, the amount of  $H_2O_2$  formed in the presence of  $O_2$  was  $\sim 0.06 \text{ mmol.L}^{-1}$ , which is  $\sim 12$  times higher than that formed in the presence of Ar ( $0.005 \text{ mmol.L}^{-1}$ ). For comparison basis, a reaction was performed at a controlled temperature of 25 °C. After 30 min of irradiation, the amount of  $H_2O_2$  formed in the presence of  $O_2$  was  $\sim 0.09 \text{ mmol.L}^{-1}$ . This was significantly higher than that found at 80 °C because the formed  $H_2O_2$  did not suffer from thermal decomposition at 25 °C

We suspect that  $H_2O_2$ , although formed in a rather low concentration, was not innocent in the reaction mechanism, in particular for the generation of highly reactive  $O^*$  species (accompanied by the release of  $H_2O$ ) on the surface of  $Au/Fe_2O_3$  catalyst (presented later in Figure 9). Indeed,  $O^*$  species has been reported to be highly mobile on the surface of Au-supported catalyst<sup>46</sup> and would readily react with substrates, leading to the formation of oxidized product(s). To test this hypothesis, molecular oxygen was replaced by  $H_2O_2$  (2 mol equivalent cellulose) and we performed the sonochemical oxidation of cellulose in the presence of  $Au/Fe_2O_3$  catalyst at atmospheric pressure (reactor was purged with Ar at least three times to eliminate trace amounts of  $O_2$ ). Product analyses revealed the formation of OA with 24 % yield, together with trace amounts of gluconic acid (1.5 % yield) and 5 % of 2-keto-gluconic acid, suggesting the plausible decomposition of  $H_2O_2$  into  $O^*$  and  $H_2O$  species and further oxidative conversion of cellulose to oxalic acid under ultrasound irradiation conditions, in

the presence of Au/Fe<sub>2</sub>O<sub>3</sub> catalyst. No detectable products were formed when similar reaction was performed under silent conditions at 120 °C within 9 h of reaction and in the presence of Au/Fe<sub>2</sub>O<sub>3</sub> catalyst, showing the pivotal role of ultrasound on the activation of cellulose.

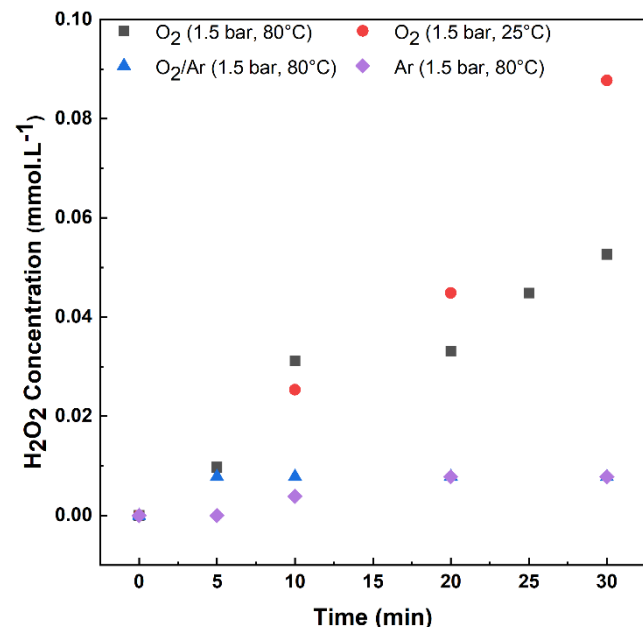


**Figure 6.** Formation rate of H<sub>2</sub>O<sub>2</sub> in the presence of different gases, determined by UV-VIS spectrophotometry. Reaction conditions: 15mL of H<sub>2</sub>O, temperatures = 25 °C and 80 °C.

To further confirm this postulation, X-ray photoelectron spectroscopy (XPS) technique was carried out to gain insights about the surface valance state of the Au nanoparticles, before and after ultrasonic irradiation in the presence of O<sub>2</sub>. **Figure 7** shows the Au 4f spectra of the fresh (**Fig. 7a**) and spent Au/Fe<sub>2</sub>O<sub>3</sub> (**Fig. 7b**) catalysts, which were deconvoluted by using a Gaussian peak fitting method. For the fresh catalyst, the peaks at ~84.0 and 87.7 eV were assigned to Au 4f<sub>7/2</sub> and Au 4f<sub>5/2</sub> of Au<sup>0</sup>, respectively, confirming the presence of Au nanoparticles in its metallic state on the surface of Fe<sub>2</sub>O<sub>3</sub> support. The XPS of the spent Au/Fe<sub>2</sub>O<sub>3</sub> catalyst revealed the appearance of a thin layer of gold oxide in the form Au<sub>2</sub>O<sub>3</sub>. This was supported, after deconvolution of the spectrum, by two pairs of signals appearing at 83.9 eV, 87.5 eV and 85.2 eV and 88.8 eV, as shown in **Figure 7b**. This analysis reveals that Au exists in two different oxidations states of Au<sup>0</sup> and Au<sup>3+</sup> after ultrasonic irradiation. This oxidation of Au might be explained by the generation of highly reactive O\* species under ultrasonic irradiation. Furthermore, this partial oxidation of Au further provides an indirect evidence of the extreme conditions generated

during the cavitation bubble implosion, because the oxidation of Au either partially or totally, often usually requires very high temperatures (> 350 °C).<sup>46, 47</sup>

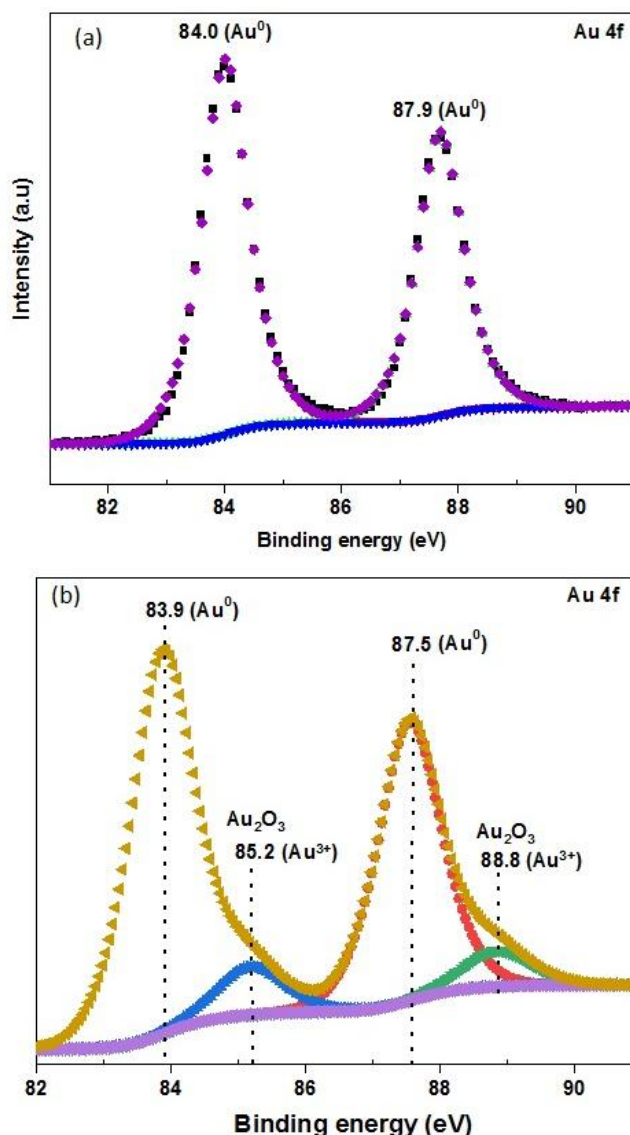


**Figure 7.** XPS analysis of Au 4f of (a) as-prepared Au/Fe<sub>2</sub>O<sub>3</sub> and (b) spent-Au/Fe<sub>2</sub>O<sub>3</sub> catalyst recovered after ultrasound irradiation (0.025g Au/Fe<sub>2</sub>O<sub>3</sub>, 15 mL water, 0.15 MPa O<sub>2</sub> pressure, 9 h reaction time).

The structural integrity of the catalyst was next investigated. SEM analyses were performed on the Au/Fe<sub>2</sub>O<sub>3</sub> fresh and spent catalysts (**Figure 8a** and **8b**, respectively). The SEM results did not reveal any significant differences between the fresh and spent catalysts. This demonstrates that ultrasound irradiation did not impact significantly the structural integrity of the Au/Fe<sub>2</sub>O<sub>3</sub> catalyst. We further investigated the impact of ultrasound irradiation on the size of Au particles by performing TEM analyses on both the fresh and spent Au/Fe<sub>2</sub>O<sub>3</sub> catalysts. The fresh Au/Fe<sub>2</sub>O<sub>3</sub> catalyst was found to

have an average particle size of 3.42 nm, and that of the spent catalyst was 3.12 nm. These results reveal that that ultrasound irradiation did not significantly impact the size of Au nanoparticles. The atomic percentage of Au after reaction was found to be 0.81 %. This was not significantly different from the fresh sample (0.9 %), which suggest there was no significant leaching or loss of Au to the reaction solution.

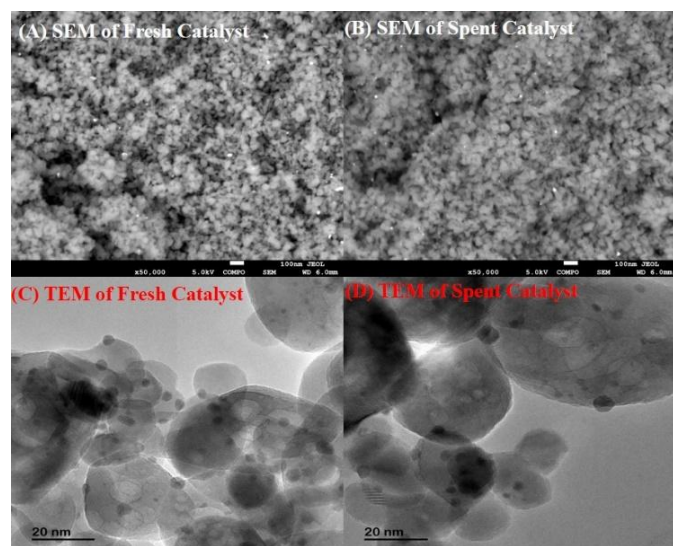


**Figure 8.** (A) SEM image of Fresh catalyst, (B) SEM image of Spent catalyst, (C) TEM image of Fresh catalyst, (D) TEM image of Spent catalyst.

To gain more fundamental insights about the reaction taking place on the Au/Fe<sub>2</sub>O<sub>3</sub> catalytic surface, we performed DFT calculations using the VASP code. Experimental data have confirmed that Fe<sub>2</sub>O<sub>3</sub> is inactive in the oxidative depolymerisation of cellulose under ultrasonic conditions, and deposition of Au was necessary to promote the oxidation reaction. On the other hand, unsupported Au is known for its low oxidation activity,<sup>48, 49</sup> mainly due to its low affinity for oxygen species and also to high energy barriers to activate O<sub>2</sub> on Au (presented in **Figure 9** and more details in the **Supporting Information**). Therefore, we focused our calculations on the properties of the interfacial sites between Au nanoparticles and the Fe<sub>2</sub>O<sub>3</sub> support to understand the activity of this material. First, we calculated the adhesion energies and Bader charges for Au(111) overlayer films on Fe<sub>2</sub>O<sub>3</sub> support with different overlayer thicknesses (one, two and 3 atomic layers) (**Table 2**). Besides, the charge density differences for those structures were also plotted in the **Supporting Information**. The observed data are used to evaluate the electronic properties of Au atoms at different proximity from the Fe<sub>2</sub>O<sub>3</sub> surface in the fresh Au/Fe<sub>2</sub>O<sub>3</sub> catalyst and

how their chemistry was modified due to the interaction with the support.

**Table 2.** Adhesion energy using equation (3) and computed Bader charge of Au atoms for Au overlayer films on Fe<sub>2</sub>O<sub>3</sub> support.

Systems	Average/Differential adhesion energy (eV)	Bader charge of Au atoms	
1 Au layer on Fe <sub>2</sub> O <sub>3</sub>	-3.27	0.25 ± 0.02	
2 Au layers on Fe <sub>2</sub> O <sub>3</sub>	-3.51/-3.75	Layer 1	0.28 ± 0.01
		Layer 2	-0.02 ± 0.01
3 Au layers on Fe <sub>2</sub> O <sub>3</sub>	-3.60/-3.78	Layer 1	0.25 ± 0.02
		Layer 2	0.02 ± 0.01
		Layer 3	-0.02 ± 0.01
Au(111)	-3.78	-0.03	

The computed adhesion energy of a monolayer Au(111) film on Fe<sub>2</sub>O<sub>3</sub> was -3.27 eV. At the interface between Au monolayer film and Fe<sub>2</sub>O<sub>3</sub> support, the charge is transferred from Au over-layer to the support, resulting in a positive charge of +0.25 for Au atoms (**Table 2**). Major of the charges transferred from Au are accumulated in the surface lattice oxygen's of Fe<sub>2</sub>O<sub>3</sub>, and only small amount of charge is further transferred to underneath Fe and lattice oxygen atoms. It could be visualized in the charge density difference plot shown in **Figure S10 (SI)**, that the charge depletion regions (presented in blue colour) were localized in the Au over layer, consistent with the positive charges implemented on those Au atoms. The electron densities are accumulated at the Au-Fe<sub>2</sub>O<sub>3</sub> interface (green colour regions), reflecting the charge transfer from Au to Fe<sub>2</sub>O<sub>3</sub>. However, regarding the bilayer and tri-layer of Au films supported on Fe<sub>2</sub>O<sub>3</sub>, the computed adhesion energies became stronger with values of -3.51 and -3.60 eV, respectively (**Table 2**). It is important to mention that the differential adhesion energy (energy to adhere one more Au layer on existing over layer of Au/Fe<sub>2</sub>O<sub>3</sub>) of the bilayer (-3.75 eV) and tri layer (-3.78 eV) are very close to the adhesion energy of Au film on pure Au(111) (-3.78 eV, **Table 2**), suggesting that the Au atoms in the 2<sup>nd</sup> and 3<sup>rd</sup> layer above the interface might have chemical properties similar to surface metallic Au atoms of pure Au(111). Computed Bader charges also support this claim (**Table 2**). Indeed, Au atoms in the top layer of

the bilayer and tri-layer Au(111) on Fe<sub>2</sub>O<sub>3</sub> have a charge of -0.02; almost the same as the charge on unsupported Au(111) surface (-0.03). Only the Au atoms in the 1<sup>st</sup> layer directly above Fe<sub>2</sub>O<sub>3</sub> is positively charged. To our knowledge, this is the first example of charge transfer from Au to Fe<sub>2</sub>O<sub>3</sub>, previous reports being focussed on TiB<sub>2</sub> or TiO<sub>2</sub> supports.<sup>50, 51</sup> One should note that the charge transfer between Au and Fe<sub>2</sub>O<sub>3</sub> occurred with a much higher magnitude than with previously reported supports, highlighting the strong ability of Fe<sub>2</sub>O<sub>3</sub> in modifying the electronic properties, and thus the catalytic activity, of supported Au atoms. Further demonstrating that the interface Au-Fe<sub>2</sub>O<sub>3</sub> is more likely to play a major role in the cellulose depolymerisation oxidation reaction mechanism.

As it has been observed in previous reports, atomic oxygen species play key roles in facilitating oxidative reactions on metal/metal

oxides catalysts.<sup>52, 53</sup> To understand the generation of atomic oxygen at the Au-Fe<sub>2</sub>O<sub>3</sub> interface, we evaluated the binding energies of key species adsorbed on the monolayer of Au film on Fe<sub>2</sub>O<sub>3</sub>, including H\*, OH\*, O<sub>2</sub>, OOH\*, H<sub>2</sub>O<sub>2</sub> and H<sub>2</sub>O (\* denotes the adsorbed state of the intermediate). The results are shown in **Figure 9a**. Besides, the binding energies of those intermediates on pure Au (111) surface are also presented to emphasize the synergistic role of Au and Fe<sub>2</sub>O<sub>3</sub> in facilitating the formation of O\*. As a general trend, the more positive the energy values, the weaker the binding interaction of those intermediates. As it could be seen, all the intermediates adsorb weakly on pure Au (111) surface, and the formations of H\*, O\*, H<sub>2</sub>O<sub>2</sub> and OOH\* on Au(111) surface are even thermodynamically unfavourable, as illustrated by their positive binding energy (**Figure 9a**). Those data support that pure Au is inactive to generate active oxygen species that are needed to catalyse the cellulose oxidation.

## ARTICLE

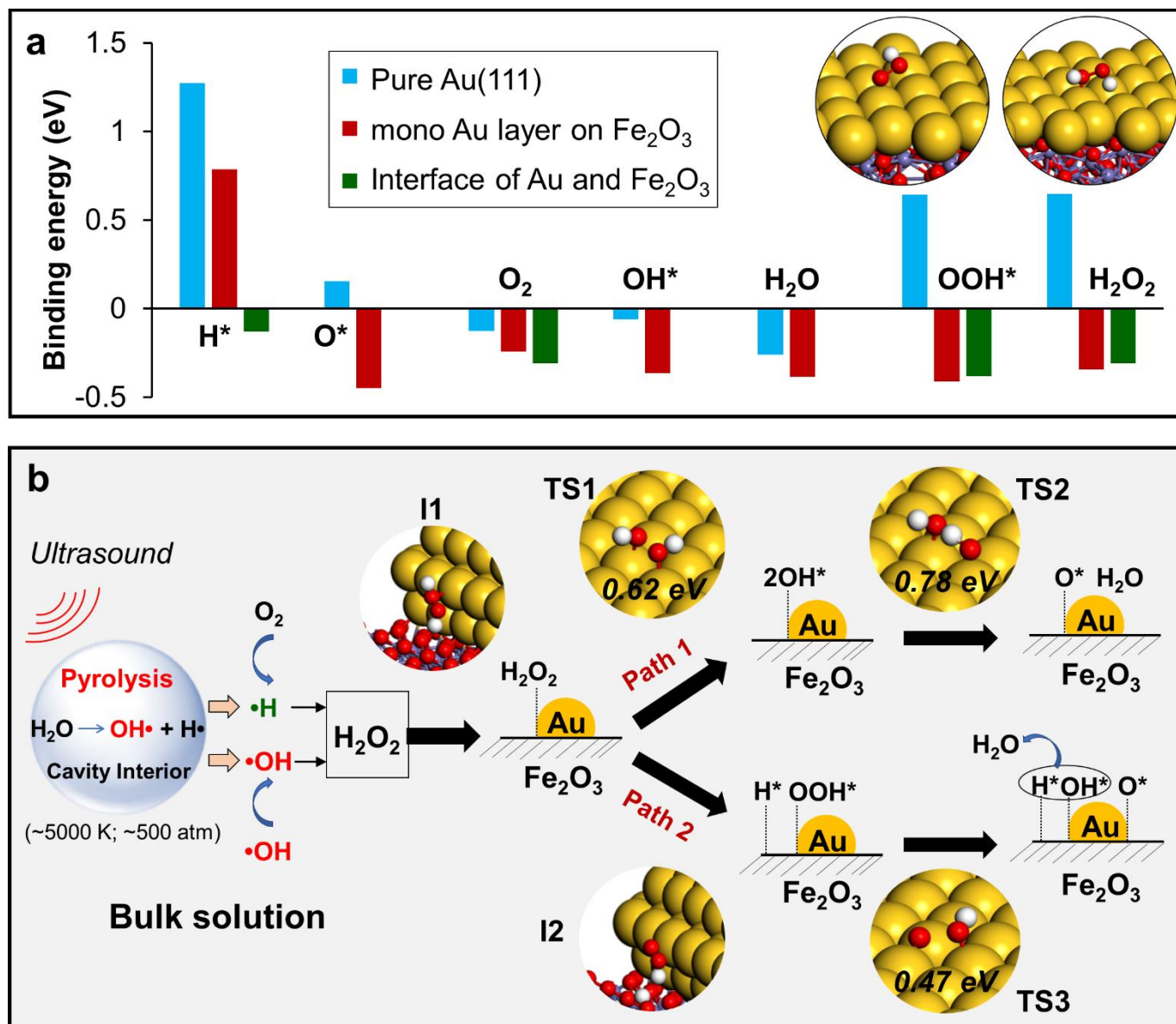


**Figure 9.** (a) Binding energies of molecules and species on Au(111); monolayer Au/Fe<sub>2</sub>O<sub>3</sub> and at the interfacial site; (b) Formation of high active oxygen species on Au/Fe<sub>2</sub>O<sub>3</sub> in the presence of ultrasound irradiation.

In contrast, on the surface of monolayer of Au supported on Fe<sub>2</sub>O<sub>3</sub> (equivalent to Au sites directly coordinated at the interface with Fe<sub>2</sub>O<sub>3</sub>), those intermediates adsorb stronger but to different extent. The binding energies of O<sub>2</sub> and H<sub>2</sub>O on the monolayer of Au on Fe<sub>2</sub>O<sub>3</sub> are slightly enhanced by 0.12 and 0.13 eV, respectively. However, surface hydroxyl (OH\*), atomic oxygen (O\*), H<sub>2</sub>O<sub>2</sub> and hydroperoxyl (OOH\*) are much stronger stabilized on monolayer of Au/Fe<sub>2</sub>O<sub>3</sub>

than on pure Au (111) surface by magnitudes larger of -0.31, -0.60, -0.99 and -1.06 eV, respectively (Figure 9a). As a result, the formations of those species are all thermodynamically favourable. The strong adsorptions of those oxygen species are correlated with the positive charges implemented on the Au sites induced by the interaction with Fe<sub>2</sub>O<sub>3</sub> support.<sup>51, 54-56</sup> However, the activation of O<sub>2</sub> to produce active oxygen O\*, is still difficult with an energy barrier

of 1.28 eV. Therefore  $O^*$  is not likely to be formed directly from  $O_2$ . We next evaluated the binding of  $H^*$  at the interface between Au and the  $Fe_2O_3$  support. It could be seen that  $H^*$  binds much stronger on lattice oxygen atom of  $Fe_2O_3$  at the interfacial Au- $Fe_2O_3$  site (structure I2, Fig. 9b) and results in an enhancement on thermodynamic driving force either for the abstraction of hydrogen from  $H_2O_2$  or for the recombination of  $H^*$  and  $O_2$  to form  $OOH^*$  which is further decomposed easily to generate atomic oxygen with low activation barrier of 0.47 eV. Therefore, the synergy between Au and  $Fe_2O_3$  in catalysing cellulose oxidation are: (i) charge transfer between Au and  $Fe_2O_3$  inducing positive charge on Au atoms at the interface, thermodynamically stabilizing the high active oxygen species ( $O^*$ ,  $OH^*$  and  $OOH^*$ ) required for the cellulose oxidation<sup>26, 57, 58</sup> and (ii) strongly adsorption of  $H^*$  at the interfacial sites, kinetically facilitating the formation of  $OOH^*$  intermediate either from  $H_2O_2$  abstraction or  $O_2$  hydrogenation, which subsequently decompose to active atomic oxygen and  $OH^*$  species.

Finally, we perform DFT calculations to propose a plausible reaction mechanism (Figure 9b). As described in the previous section, the reaction is initiated by the sonolysis of water (formation of  $H^\bullet$  and  $OH^\bullet$ ) resulting in the formation of  $H_2O_2$  in Figure 6. The generated  $H_2O_2$  adsorbs strongly at the Au- $Fe_2O_3$  interface (structure I1, Fig. 9b). Adsorbed  $H_2O_2$  could be further decomposed via two different pathways to generate atomic oxygen. In the first path (Path 1 in Fig. 9b),  $H_2O_2$  is dissociated with the activation barrier of 0.62 eV (TS1 in Fig. 7b) into two  $OH^*$  fragments, also stabilized at the interface of Au/ $Fe_2O_3$ . It should be noted that without the catalyst, this reaction has an extremely high barrier of about 2.16 eV as was reported in both earlier theoretical and experimental studies.<sup>59, 60</sup> Two  $OH^*$  species can then cross-react with each other to form  $H_2O$  and release the active oxygen radical  $O^*$  with a barrier of 0.78 eV (TS2, Fig. 9b). In pathway 2,  $H^*$  is directly abstracted from the *in-situ* generated  $H_2O_2$  molecule by the lattice oxygen of  $Fe_2O_3$  support and produces  $OOH^*$  which adsorbs strongly on interfacial Au/ $Fe_2O_3$  site (IS2 in Fig. 9b). This step is barrier-less. Once  $OOH^*$  is formed, it could be activated easily on positive charged Au site at the interface between Au nanoparticle and  $Fe_2O_3$  with a barrier of 0.47 eV, forming the  $O^*$  and  $OH^*$  species (TS3, Fig. 9b). The generated  $OH^*$  then can combine with  $H^*$ , releasing water molecule. It could be seen that both pathway 1 and 2 resulted in the formation of active

oxygen species  $O^*$ , consistent with the XPS data reported in Figure 7. However, owing to lower barriers, the decomposition of  $H_2O_2$  via the formation of  $OOH^*$  in pathway 2 is a more favourable scenario.

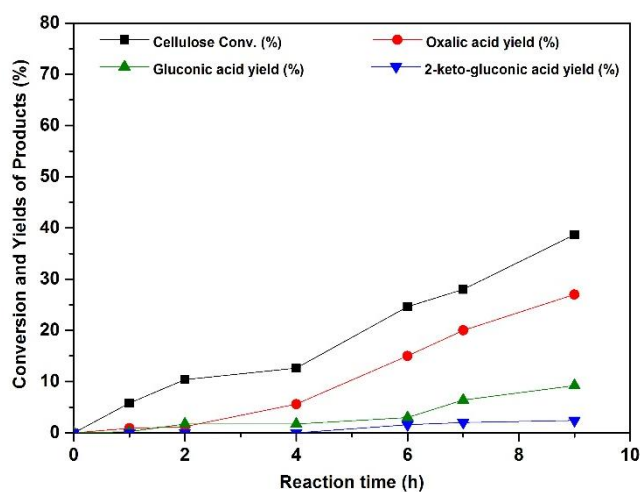


**Figure 10.** Irradiation time course for cellulose conversion over Au/CuO catalyst. Reaction conditions: 0.2g Cellulose, 15 mL water, 0.02g Catalyst, 1-9h reaction time.

To further confirm the important role of the Au- $Fe_2O_3$  interactions, gold nanoparticles were supported on copper-oxide (CuO). Our DFT calculations showed that the computed adhesion energy of a monolayer of Au supported on CuO is only -3.02 eV (Supporting information), much weaker than the computed adhesion energy of a monolayer of Au supported on  $Fe_2O_3$  (-3.27 eV, Table 2). The charge transfer between Au and CuO also induces positive charges on support Au atoms but with much lower magnitude, *i.e.* Au atoms in the atomic layer directly at the interface of Au/CuO gained a positive charge of 0.13, compare to 0.22 for Au/ $Fe_2O_3$  (Table 2). In line with these DFT calculations, we conducted the oxidation of cellulose using the Au/CuO catalysts and under ultrasonic irradiation (0.15 MPa of  $O_2$ ) and the results are presented in Figure 10. The yields of OA obtained over the Au/CuO catalyst were significantly lower than those obtained over Au/ $Fe_2O_3$ , further highlighting the significant role of the Au-support interaction. Indeed, OA was formed with only 10 % yield (conv. Cellulose = 20 %, selectivity = 50%) after 6 h of ultrasonic irradiation in the presence of Au/CuO while it was 24 % yield (conv. Cellulose 38 %, selectivity = 63%) over the Au/ $Fe_2O_3$ .

## Conclusion

We demonstrated here that ultrasonic irradiation at 20 kHz and under low pressure of oxygen in the presence of Au/ $Fe_2O_3$  catalyst

promoted the catalytic conversion of cellulose to organic acids, in particular oxalic acid. Under optimized conditions, an overall oxalic acid yield of 45 % was achieved, corresponding to an overall yield of 53% into carboxylic acids (gluconic, formic, 2-keto-gluconic acid, etc.) at a conversion of 55 % of cellulose. Characterization techniques (XRD and SEM) confirmed that, although sonication did not significantly alter the crystallinity of the cellulose, localised heating and hotspots (thanks to intense shockwaves generated) induced the partial fragmentation of cellulose particles, making it more reactive for further oxidative catalytic conversion into OA. Density functional theory (DFT) calculations was performed to characterize the interfacial sites between Au nanoparticle and Fe<sub>2</sub>O<sub>3</sub> support. The charge transfer between Au layer and Fe<sub>2</sub>O<sub>3</sub> support induces positive charge on exposed Au atoms, which are majorly confined within the first Au layer closest to the interface. The stronger binding energies of the key intermediates (O\*, OH\* and OOH\*) on these positively charged Au sites provide thermodynamic driving force for the formation of atomic oxygen and results in the high activity of Au/Fe<sub>2</sub>O<sub>3</sub> catalyst for cellulose oxidation.

At the stage of our investigations, full elucidation of the reaction mechanism requires further investigations. Although we proposed that *in situ* produced H<sub>2</sub>O<sub>2</sub> may play a key role, its formation remains, however, rather low and it cannot explain, on its own, the rate of reaction we observed. Under ultrasonic conditions, we suspect that other phenomena could be considered such as over-heating of the catalyst surface at the bubble collapse time or direct sono-activation of O<sub>2</sub> which is hardly feasible under conventional catalytic conditions. This is the topic of current investigations in our group.

## Acknowledgement

Authors are grateful to the CNRS, the University of Poitiers and the ANR JCJC AminoSound project ID ANR-20-CE07-0006 for funding this research work. Q. T. T. and J. Z. would like to acknowledge the financial support from A\*STAR AME IAF-PP grant (Grant No. A19E9a0103) and high-performance computational facilities from the National Supercomputing Centre (NSCC) Singapore (<https://www.nsc.sg>) and A\*STAR Computational Resource Centre (A\*CRC).

## Conflicts of interest

There are no conflicts to declare.

## References

1. P. Fordham, M. Besson and P. Gallezot, *Applied Catalysis A: General*, 1995, **133**, L179-L184.
2. A. Villa, C. Campione and L. Prati, *Catalysis Letters*, 2007, **115**, 133-136.
3. J. Cai, H. Ma, J. Zhang, Z. Du, Y. Huang, J. Gao and J. Xu, *Chinese Journal of Catalysis*, 2014, **35**, 1653-1660.
4. *Global Industry Analysts*, 2008. (<http://www.strategyr.com/PressMCP-2105.asp>)
5. E. Betiku, H. A. Emeko and B. O. Solomon, *Heliyon*, 2016, **2**.
6. X. Jin, M. Zhao, C. Zeng, W. Yan, Z. Song, P. S. Thapa, B. Subramaniam and R. V. Chaudhari, *ACS Catalysis*, 2016, **6**, 4576-4583.
7. C. Xu, Y. Du, C. Li, J. Yang and G. Yang, *Applied Catalysis B: Environmental*, 2015, **164**, 334-343.
8. S. A. Kondrat, P. J. Miedziak, M. Douthwaite, G. L. Brett, T. E. Davies, D. J. Morgan, J. K. Edwards, D. W. Knight, C. J. Kiely, S. H. Taylor and G. J. Hutchings, *ChemSusChem*, 2014, **7**, 1326-1334.
9. H. Kimura, A. Kimura, I. Kokubo, T. Wakisaka and Y. Mitsuda, *Applied Catalysis A: General*, 1993, **95**, 143-169.
10. D. Liang, J. Gao, J. Wang, P. Chen, Y. Wei and Z. Hou, *Catalysis Communications*, 2011, **12**, 1059-1062.
11. T. van Haasterecht, T. W. van Deelen, K. P. de Jong and J. H. Bitter, *Catalysis Science & Technology*, 2014, **4**, 2353-2366.
12. M. D. Mathew, M. Gopal and S. K. Banerjee, *Agricultural Wastes*, 1984, **11**, 47-59.
13. D. F. Othmer, C. H. Gamer and J. J. Jacobs, *Industrial & Engineering Chemistry*, 1942, **34**, 262-267.
14. J. M. Krochta, S. J. Tillin and J. S. Hudson, *Applied Biochemistry and Biotechnology*, 1988, **17**, 23-32.
15. M. Benoit, A. Rodrigues, Q. Zhang, E. Fourré, K. De Oliveira Vigier, J.-M. Tatibouët and F. Jérôme, *Angewandte Chemie International Edition*, 2011, **50**, 8964-8967.
16. A. Karam, P. N. Amaniampong, J. M. García Fernández, C. Oldani, S. Marinkovic, B. Estrine, K. De Oliveira Vigier and F. Jérôme, *Frontiers in Chemistry*, 2018, **6**.
17. J. Fan, M. De bruyn, V. L. Budarin, M. J. Gronnow, P. S. Shuttleworth, S. Breeden, D. J. Macquarrie and J. H. Clark, *Journal of the American Chemical Society*, 2013, **135**, 11728-11731.
18. V. S. Moholkar, M. M. C. G. Warmoeskerken, C. D. Ohl and A. Prosperetti, *AIChE Journal*, 2004, **50**, 58-64.
19. R. C. Sun, X. F. Sun and X. H. Ma, *Ultrasonics Sonochemistry*, 2002, **9**, 95-101.
20. R. Velmurugan and K. Muthukumar, *Bioresource Technology*, 2011, **102**, 7119-7123.
21. A. García, M. G. Alriols, R. Llano-Ponte and J. Labidi, *Bioresource Technology*, 2011, **102**, 6326-6330.



22. Z. Jiang, Z. Zhang, J. Song, Q. Meng, H. Zhou, Z. He and B. Han, *ACS Sustainable Chemistry & Engineering*, 2016, **4**, 305-311.
23. E. Kuna, R. Behling, S. Valange, G. Chatel and J. C. Colmenares, *Topics in Current Chemistry*, 2017, **375**, 41.
24. Q. T. Trinh, A. Banerjee, K. B. Ansari, D. Q. Dao, A. Drif, N. T. Binh, D. T. Tung, P. M. Q. Binh, P. N. Amaniampong, P. T. Huyen and M. T. Le, in *Biorefinery of Alternative Resources: Targeting Green Fuels and Platform Chemicals*, eds. S. Nanda, D.-V. N. Vo and P. K. Sarangi, Springer Singapore, Singapore, 2020, DOI: 10.1007/978-981-15-1804-1\_14, pp. 317-353.
25. N. Kardos and J.-L. Luche, *Carbohydrate Research*, 2001, **332**, 115-131.
26. P. N. Amaniampong, Q. T. Trinh, K. De Oliveira Vigier, D. Q. Dao, N. H. Tran, Y. Wang, M. P. Sherburne and F. Jérôme, *Journal of the American Chemical Society*, 2019, **141**, 14772-14779.
27. G. Kresse and J. Hafner, *Physical Review B*, 1993, **47**, 558-561.
28. G. Kresse and J. Furthmüller, *Computational Materials Science*, 1996, **6**, 15-50.
29. Q. T. Trinh, K. Bholá, P. N. Amaniampong, F. Jérôme and S. H. Mushrif, *The Journal of Physical Chemistry C*, 2018, **122**, 22397-22406.
30. R. B. Wang and A. Hellman, *The Journal of Chemical Physics*, 2018, **148**, 094705.
31. A. Mahmoud, P.-M. Deleuze and C. Dupont, *The Journal of Chemical Physics*, 2018, **148**, 204701.
32. S. Grimme, J. Antony, S. Ehrlich and H. Krieg, *The Journal of Chemical Physics*, 2010, **132**, 154104.
33. S. K. Shaikhutdinov and W. Weiss, *Surface Science*, 1999, **432**, L627-L634.
34. M.-T. Nguyen, N. Seriani, S. Piccinin and R. Gebauer, *The Journal of Chemical Physics*, 2014, **140**, 064703.
35. M.-T. Nguyen, S. Piccinin, N. Seriani and R. Gebauer, *ACS Catalysis*, 2015, **5**, 715-721.
36. W. Tang, E. Sanville and G. Henkelman, *Journal of Physics: Condensed Matter*, 2009, **21**, 084204.
37. G. Henkelman, A. Arnaldsson and H. Jónsson, *Computational Materials Science*, 2006, **36**, 354-360.
38. P. N. Amaniampong, Q. T. Trinh, B. Wang, A. Borgna, Y. Yang and S. H. Mushrif, *Angewandte Chemie International Edition*, 2015, **54**, 8928-8933.
39. P. N. Amaniampong, Q. T. Trinh, J. J. Varghese, R. Behling, S. Valange, S. H. Mushrif and F. Jérôme, *Green Chemistry*, 2018, **20**, 2730-2741.
40. C. W. Han, T. Choksi, C. Milligan, P. Majumdar, M. Manto, Y. Cui, X. Sang, R. R. Unocic, D. Zemlyanov, C. Wang, F. H. Ribeiro, J. Greeley and V. Ortalan, *Nano Letters*, 2017, **17**, 4576-4582.
41. H. Wang, L. Wang, D. Lin, X. Feng, Y. Niu, B. Zhang and F.-S. Xiao, *Nature Catalysis*, 2021, **4**, 418-424.
42. T. García, J. M. López, B. Solsona, R. Sanchis, D. J. Willock, T. E. Davies, L. Lu, Q. He, C. J. Kiely and S. H. Taylor, *ChemCatChem*, 2019, **11**, 1915-1927.
43. Q. Zhang, M. Benoit, K. De Oliveira Vigier, J. Barrault, G. Jégou, M. Philippe and F. Jérôme, *Green Chemistry*, 2013, **15**, 963-969.
44. M.-F. Zhang, Y.-H. Qin, J.-Y. Ma, L. Yang, Z.-K. Wu, T.-L. Wang, W.-G. Wang and C.-W. Wang, *Ultrasonics Sonochemistry*, 2016, **31**, 404-408.
45. C. Gong and D. P. Hart, *The Journal of the Acoustical Society of America*, 1998, **104**, 2675-2682.
46. P. N. Amaniampong, K. Li, X. Jia, B. Wang, A. Borgna and Y. Yang, *ChemCatChem*, 2014, **6**, 2105-2114.
47. A. Zhang, L. Zhang, G. Jing, H. Zhang, S. Wang, H. Su and S. Zeng, *International Journal of Hydrogen Energy*, 2018, **43**, 10322-10333.
48. M. Haruta, *The Chemical Record*, 2003, **3**, 75-87.
49. B. Hammer and J. K. Nørskov, *Nature*, 1995, **376**, 238-240.
50. R. Li, Z. Liu, Q. T. Trinh, Z. Miao, S. Chen, K. Qian, R. J. Wong, S. Xi, Y. Yan, A. Borgna, S. Liang, T. Wei, Y. Dai, P. Wang, Y. Tang, X. Yan, T. S. Choksi and W. Liu, *Advanced Materials*, 2021, **33**, 2101536.
51. G. Liu, P. R. Narangari, Q. T. Trinh, W. Tu, M. Kraft, H. H. Tan, C. Jagadish, T. S. Choksi, J. W. Ager, S. Karuturi and R. Xu, *ACS Catalysis*, 2021, **11**, 11416-11428.
52. M. McEntee, W. Tang, M. Neurock and J. T. Yates, *ACS Catalysis*, 2015, **5**, 744-753.
53. I. X. Green, M. McEntee, W. Tang, M. Neurock and J. T. Yates, *Topics in Catalysis*, 2013, **56**, 1512-1524.
54. I. X. Green, W. Tang, M. Neurock and J. T. Yates, *Accounts of Chemical Research*, 2014, **47**, 805-815.
55. Y.-G. Wang, Y. Yoon, V.-A. Glezakou, J. Li and R. Rousseau, *Journal of the American Chemical Society*, 2013, **135**, 10673-10683.
56. Q. T. Trinh, J. Yang, J. Y. Lee and M. Saeys, *Journal of Catalysis*, 2012, **291**, 26-35.
57. C.-R. Chang, X.-F. Yang, B. Long and J. Li, *ACS Catalysis*, 2013, **3**, 1693-1699.
58. G. M. Mullen, L. Zhang, E. J. Evans, T. Yan, G. Henkelman and C. B. Mullins, *Journal of the American Chemical Society*, 2014, **136**, 6489-6498.
59. T. Tsuneda and T. Taketsugu, *Physical Chemistry Chemical Physics*, 2018, **20**, 24992-24999.
60. P. Gray, *Transactions of the Faraday Society*, 1959, **55**, 408-417.